Plasma Treatment Optimizes Proton, Electron and Mass Transport in Low-Iridium Catalyst Layers for Water Electrolysis

Yuyang Wang, [†a] Liulin Que, [†a] Qichao Fan, [a] Jian Huang,[*a] Haokai Xu, [a] Dingding Ye, [a] Xianqing Zhu, [a] Jun Li,[*a] Xun Zhu, [a] and Qiang Liao, [a]

[a] Key Laboratory of Low-grade Energy Utilization Technologies and Systems, National Innovation Center for Industry-Education Integration of Energy Storage Technology, School of Energy and Power Engineering, Chongqing University, Ministry of Education, Chongqing, 400044, China

* Corresponding author

[a] E-mail: cquhj@cqu.edu.cn (Jian Huang), lijun@cqu.edu.cn (Jun Li)

CONTENTS

■ Methods

ACL preparation:

Commercial IrO_2 (99.9 %, Ir≥84.5%, Alfa Aesar, U.S.) and Pt/C (40wt%, Johnson Matthey, UK) powders were used as oxygen and hydrogen evolution electrocatalysts, respectively. Catalyst inks were fabricated by dispersing the IrO_2 or Pt/C powder within the two PFSA suspension, DI water (18.2 MΩ·cm), and 1-propanol (AR, Chengdu Kelong Chemical Co., Ltd, China). In the anode catalyst ink, the mass ratio of IrO_2 to PFSA ionomer is 7:1, and the volume ratio of H_2O to 1-propanol is 1:2. In the cathode catalyst ink, the mass ratio of IrO_2 to PFSA ionomer is 5:1, and the volume ratio of H_2O to 1-propanol is 1.4:1. The fresh ink was first subjected to ultrasonicate for 20 minutes and then sprayed onto a Nafion 212 membrane by an ultrasonic spray system (SimCoat, Sono-Tek Corporation, U.S.), with a pump rate of 0.3 $mL \cdot min^{-1}$ and a heating plate temperature of 90℃. The cathode and anode CL were sprayed sequentially at an interval of 30 min to ensure complete removal of the solvent from the CL. The final Ir loadings obtained for the ACL were 0.4 $mg \cdot cm^{-2}$, and the Pt loadings for the cathodic catalytic layer were also 0.2 $mg \cdot cm^{-2}$. To obtain the P-ACL, the ACL of the prepared MEA was treated using low-temperature oxygen plasma equipment (Shenzhen Shenguangda Technology Co., Ltd.) for 10 cycles, with each cycle consisting of a 5-second plasma exposure followed by a 5-second cooling interval.

Characterizations

X-ray diffraction (XRD) was conducted by a BRUCKER D8 ADVANCE X-ray powder diffractometer with monochromatized Cu Kα radiation. X-ray photoelectron spectroscopy (XPS) and ultraviolet photoelectron spectroscopy (UPS) were operated with Thermo Escalab 250Xi. The scanning electronic microscopy (SEM) images were obtained by a Hitachi SU8020 electron microscope. AFM in air condition was conducted at C-AFM and QNM in Air Model with a nitride-coated silicon tip on nitride cantilever (Dimension; Bruker, Germany). The physicochemical properties of the ionomer thin films were characterized by Fourier transform infrared spectroscopy (FTIR, Nicolet 6700, Thermo Fisher Scientific, Waltham, U.S.) over the range of 2000–400 cm^{-1}.

Electrochemical test:

A commercial electrolyzer with a 6.8-cm^2 active area (Mainz-PEM04, Mainz Laboratory Equipment Co., Ltd. Shandong, China) was utilized to evaluate the PEMWE performance. Titanium-fiber felts (~240-μm thickness, 50% porosity, Bekaert Co., Ltd., Zwevegem, Belgium) were used as PTLs at the cathode and anode sides. A 230-μm-thick PTFE film was used as a gasket, and the electrolyzer was assembled using a torque of 4 Nm (with a M5 bolt). Following the assembly of the electrolyzer, water is fed through the system for 3 hours to facilitate electrode activation. Electrochemical tests were performed using an electrochemical workstation equipped with a potentiostat and booster (VMP-300 & 80A Booster, Bio-Logic, Seyssinet-

Pariset, France). All testing procedures were operated with a water flow rate of 10.0 $mL \cdot min^{-1}$. Electrochemical impedance spectra measurements were made in the range of 0.05 Hz-100 kHz with the current perturbations of ±200 mA to determine the high frequency resistance (HFR), charge, and mass transport impedance of different MEAs.

AIMD calculations

All AIMD calculations were performed using the Vienna Ab initio Simulation Package (VASP), employing the projector-augmented wave (PAW) method to describe the electron-ion interactions. The system consisted of an IrO_2 (110) surface slab model with adsorbed H_2O and O_2 molecules, simulated under AIMD conditions to investigate the water network dynamics. The exchange-correlation functional was treated within the generalized gradient approximation (GGA) using the Perdew-Burke-Ernzerhof (PBE) form, unless otherwise specified. The precision was set to Normal (PREC= Normal) for computational efficiency, with a plane-wave energy cutoff of 400 eV.

CFD calculations

In this study, a three-dimensional, multi-physics model was developed using COMSOL Multiphysics 6.2. The simulations were performed on a workstation equipped with a six-core, 2.5 GHz Intel processor and 32 GB of RAM. The model incorporates coupled physical phenomena, including electrochemical reactions, two-phase flow, heat transfer, water transport, species transport, and hydrogen crossover,

by integrating the corresponding modules within the software. The governing equations were solved using the PARDISO direct solver with a segregated solution approach. A voltage sweep from 1.2 V to 2.0 V was applied with an increment of 0.05 V. The computational domain was discretized using a mesh consisting of 790,378 nodes to ensure solution accuracy while maintaining computational efficiency. Geometry parameters and other model parameters are listed in Table S1. The boundary condition is listed in Table S2.

Model assumptions:

(1) The PEMWE cell operate at steady state;

(2) The gas species are incompressible ideal gas;

(3) Porous media domains such as the membrane, PTLs, and CLs are considered homogeneous and isotropic;

(4) The flow is laminar due to the low velocity;

(5) The hydrogen generated is first in the dissolved state;

(6) OER and HER obey Butler–Volmer kinetics.

The model incorporates ten conservation equations to describe the processes in PEMWE: (i–iv) mass conservation and momentum conservation for liquid and gas phases, (v) liquid water saturation, (vi) species transport of mix gases, (vii) electronic charge, (viii) protonic charge, (ix) thermal transfer, (x) water transport in MEAs, and (xi) hydrogen crossover.

(i) Liquid-water mass conservation:

$$\nabla \cdot (\rho_l u_l) = S_l \tag{S1}$$

where ρ_l and u_l are the density and velocity of liquid water, respectively. S_l refers to the mass source term, which results from water consumption on the CLs.

(ii) Liquid-water momentum conservation:

$$\frac{\rho_l}{\varepsilon^{eff}}(u_l \cdot \nabla)\frac{u_l}{\varepsilon^{eff}} = \nabla \cdot \begin{bmatrix} -p_l I + \frac{\mu_l}{\varepsilon^{eff}}\left(\nabla u_l + (\nabla u_l)^T\right) \\ -\frac{2}{3}\frac{\mu_l}{\varepsilon^{eff}}(\nabla \cdot u_l) I \end{bmatrix} - \left\{\frac{\mu_l}{k_0 k_{rl}} + \frac{S_l}{(\varepsilon^{eff})^2}\right\} u_l \tag{S2}$$

The effective porosity is denoted by ε^{eff}, while p_l represents the liquid water pressure, the dynamic viscosity of liquid water is given as μ_l, and k_0 denotes the absolute permeability of the liquid phase, The relative permeability k_{rl} is expressed as the cube of the liquid water saturation *s*, i.e., $k_{rl}=s^3$.

(iii) Gas-phase mass conservation:

$$\nabla \cdot (\rho_g u_g) = S_g \tag{S3}$$

where ρ_g and u_g denote the density and velocity of the gas, respectively. S_g represents the mass source term, which is caused by the gas generated on the CLs.

(iv) Gas-phase momentum conservation:

$$u_g = -\frac{k_0 k_{rg}}{\mu_g}\nabla p_g \tag{S4}$$

where p_g and μ_g are the pressure and dynamic viscosity of the gas, respectively, and k_0 is the absolute permeability of the gas. This study defines the relative permeability of the gas phase as $k_{rg} = (1 - s)^3$.

(v) Liquid water saturation:

The capillary pressure in the porous region is:

$$p_c = p_l - p_g = \sigma\cos\theta\left(\frac{\varepsilon}{K_0}\right)^{0.5}J(s) \tag{S5}$$

$$J(s) = \begin{cases} 1.417(1-s) - 2.120(1-s)^2 + 1.263(1-s)^3, & 0^\circ < \theta \le 90^\circ \\ 1.417(1-s) - 2.120s^2 + 1.263s^3, & 90^\circ < \theta \le 180^\circ \end{cases} \tag{S6}$$

After rearranging Eqs. (S1), (S3), (S4) and (S5-S6), the conservation equation of liquid water saturation can be rewritten as:

$$\nabla\left(-\rho_g D_c \nabla s + \rho_g \frac{k_{rg}\mu_l}{k_{rl}\mu_g}u_l\right) = S_g \tag{S7}$$

Here, D_c is the capillary diffusion coefficient, which is expressed as:

$$D_c = \frac{\sigma\cos\theta}{\mu_g}k_{rg}(\varepsilon k_0)^{0.5}\frac{dJ(s)}{ds} \tag{S8}$$

(vi) Species transport of mix gases:

$$\nabla\cdot\left(\rho_g D_{ij}^{eff}\nabla w_i - \rho_g w_i\sum_j D_{ij}^{eff}\frac{\nabla w_j M_n}{M_j}\right) + \rho_g(u_g\cdot\nabla)w_i = S_{c,i} \tag{S9}$$

$$D_{H_2O,O_2/H_2}^{eff} = \begin{cases} 0.36\times10^{-4}\left(\frac{T}{T^{ref}}\right)^{1.5}\left(\frac{p_g^{ref}}{p_g}\right)k_{rg}\ (anode) \\ 1.24\times10^{-4}\left(\frac{T}{T^{ref}}\right)^{1.5}\left(\frac{p_g^{ref}}{p_g}\right)k_{rg}\ (cathode) \end{cases} \tag{S10}$$

In the PEMWE model, gas-phase species transport is governed by a multicomponent diffusion equation based on Fick's law. Here, D_{ij}^{eff} represent the effective gas diffusion coefficient between species *i* and *j*, and w_i denotes the mass fraction of gas species *i*.

(vii) Electronic charge:

$$\nabla\cdot\left(-\sigma_e^{eff}\nabla\phi_e\right) = S_e \tag{S11}$$

(viii) Protonic charge:

$$\nabla\cdot\left(\sigma_p\nabla\phi_p\right) = S_p \tag{S12}$$

In this context, the subscripts e and p denote electrons and proton transport, respectively. The variables S_e and S_p represent general source terms, while ϕ_e and ϕ_p correspond to the solid electrode potential and the liquid electrolyte potential, respectively. σ_e^{eff} indicates the effective conductivity of solid phase. The effective conductivity of electrolyte, σ_p, is dependent on both dissolved water content and the operating temperature of the cell:

$$\sigma_p = (0.5139\lambda - 0.326)exp\left\{1268\left(\frac{1}{T^{ref}} - \frac{1}{T}\right)\right\} \tag{S13}$$

where λ is the water content of the membrane, the reference temperature of $T^{ref}$is 353.15K.

(ix) Thermal transfer:

$$\nabla\left(\rho^{eff}C_p^{eff}uT\right) = \nabla\cdot\left(k^{eff}T\right) + S_T \tag{S14}$$

where ρ^{eff}, C_p^{eff} and k^{eff} represent the effective density, specific heat capacity and effective thermal conductivity, respectively. S_T denotes the energy source term, which includes contributions from irreversible heat, entropic heat and ohmic heat sources.

(x) Water transport in MEAs:

$$\nabla\cdot\left\{\underbrace{-\frac{D_\lambda^{eff}}{V_m}\nabla\lambda}_{diffusion} + \underbrace{\frac{n_d^w}{F}j_p}_{EOD} + \frac{\lambda}{V_m}\frac{K_{l,pem}p_{l,apem} - p_{l,cpem}}{\mu_l}{\delta_{pem}}\right\} = S_\lambda \tag{S15}$$

$$D_\lambda^{eff} = \varepsilon_{ion}^{1.5}\frac{3.842\lambda^3 - 32.03\lambda^2 + 67.74\lambda}{\lambda^3 - 2.115\lambda^2 - 33.013\lambda + 103.37}\times 10^{-10}exp\left[\frac{E_\lambda}{R}\left(\frac{1}{T^{ref}} - \frac{1}{T}\right)\right] \tag{S16}$$

where ε_{ion} is the volume of ionomer, which is discussed in the next section. V_m is the molar volume of the electrolyte, while E_λ is the activation energy for water diffusion. n_d^w and j_p are electro-osmotic drag coefficient and protonic flux.

(xi) Hydrogen crossover:

Hydrogen generated at the cathode catalytic layer (CCL) first exists in a dissolved, supersaturated state. Once its concentration exceeds the thermodynamic equilibrium, a portion precipitates to form gaseous bubbles, while the remaining dissolved hydrogen permeates across the PEM toward the anode. The total hydrogen transported via these two pathways—bubble formation and membrane crossover—equals the total amount of hydrogen electrochemically produced at the cathode:

$$\frac{i_{v,c}}{2F} = S_{bub} + S_{per} \tag{S17}$$

$$S_{bub} = k_L(c_{H_2}^{d} - c_{H_2}^{0}) \tag{S18}$$

$$c_{H_2}^{0} = \frac{p_{H_2}}{\sigma_{H_2}} \tag{S19}$$

where k_L denotes the mass transport coefficient, $c_{H_2}^{d}$(mol m^{-3}) the local dissolved hydrogen concentration, and $c_{H_2}^{Herry}$ (mol m^{-3}) the theoretical saturation concentration. The Henry coefficient, σ_{H_2}(Pa mol^{-1} cm^3), which relates the dissolved concentration to the hydrogen partial pressure p_{H_2}(Pa), can be estimated for temperatures within 0 to 100℃ and pressure up to 1 MPa by the following expression:

$$\sigma_{H_2} = \begin{cases} 7.9 \times 10^6 \exp\left(-\frac{545}{T}\right) \times \left(1 + 0.000071 p_{H_2}^3\right) & 0 \sim 45℃ \\ 8.34 \times 10^5 \exp\left(\frac{170}{T}\right) \times \left(1 + 0.000071 p_{H_2}^3\right) & 45 \sim 100℃ \end{cases} \tag{S20}$$

S_{per} is described by:

$$S_{per} = -\nabla \cdot \left(\varepsilon_{im} D_{H_2,im}^{eff} \nabla c_{H_2}^{d}\right) + \nabla \cdot \left(\varepsilon_{im} \frac{n_d^w}{F c_{H_2O}} \overrightarrow{i_m} \cdot c_{H_2}^{d}\right) + \nabla \cdot \left(\varepsilon_{pore} \vec{u}_l \cdot c_{H_2}^{d} + \frac{K_m \ \Delta p}{\mu_l \ d_{MEM}} \cdot c_{H_2}^{d}\right) \tag{S21}$$

Here, K_m represents the permeability of the membrane, μ_l is the dynamic viscosity of the solvent and Δp denotes the absolute pressure difference across the interface between the membrane and CLs. The electro-osmotic drag coefficient of water in the electrolyte is expressed as $n_d^w = 2.5\lambda/22$, where λ is the water content. Addtionally, c_{H_2O} refers to the molar concentration of water.

$$D_{H_2,im}^{eff} = 7.634 \times 10^{-6} exp(-\frac{2225.4}{T})\frac{f_v}{\tau_m} \quad \text{(S22)}$$

where f_v is the volumetric water content in ionomer calculated by $f_v = \lambda V_w/(V_m + \lambda V_w)$, τ_m is the tortuosity of the membrane calculated by $\tau_m = 1/(1 - 0.85(1 - f_v))$.

The volumetric reaction rates of the oxygen evolution reaction (OER) and hydrogen evolution reaction (HER) in the anode and cathode catalyst layers, respectively, were described using modified Butler–Volmer kinetics, accounting for the influence of local temperature and reactant concentration on electrochemical activity:

$$R_a = i_{v,a} = s^{n_s} a_{v,a} i_{0,a} e^{\left(-\frac{E_{exc}}{R}\left(\frac{1}{T} - \frac{1}{T^{ref}}\right)\right)}\left\{exp\left(\frac{\alpha_a F\eta}{RT}\right) - exp\left(\frac{-\alpha_c F\eta}{RT}\right)\right\} \quad \text{(S23)}$$

$$R_c = i_{v,c} = a_{v,c} i_{0,c} e^{\left(-\frac{E_{exc}}{R}\left(\frac{1}{T} - \frac{1}{T^{ref}}\right)\right)}\left\{exp\left(\frac{\alpha_a F\eta}{RT}\right) - exp\left(\frac{-\alpha_c F\eta}{RT}\right)\right\} \quad \text{(S24)}$$

In the expressions above, the subscripts *a* and *c* denote the anode and cathode, respectively. a_v, i_0 and $\alpha_{a/c}$ represent the specific active surface area, exchange current density and anodic/cathodic charge transfer coefficients, respectively. *F* and *R* are the Faraday and gas constants, *T* is the temperature, and E_{exc} (53.99 kJ/mol) is the activation energy for the electrode reaction. The activation overpotential, η, is defined as the difference between the ionic potential and the electronic potential:

$$\eta = \phi_e - \phi_p - E_{eq} \tag{S25}$$

The equilibrium voltage E_{eq} on the cathode is equal to zero and the equilibrium voltage can be calculated by the following equation:

$$E_{eq} = 1.229 - 9.0 \times 10^{-4}(T - 298.15) \tag{S26}$$

Other relevant source terms are listed in the Table S3.

A general PEMWE model is developed to investigate and predict the influence of different PTL structures on mass transit and cell performance. The total cell voltage V_{cell} is composed of four contributions: (i) the Nernst potential, V_{Nernst}, calculated from the Nernst equation; (ii) the activation overpotential, V_{act}; (iii) the ohmic overpotential, V_{Ohm}; and (iv) the mass transport overpotential, V_{mass}, as expressed in the following equation:

$$V_{cell} = V_{Nernst} + V_{act} + V_{Ohm} + V_{mass} \tag{S27}$$

(i) Nernst voltage:

$$V_{Nernst} = E_{eq} \tag{S28}$$

(ii) Activation overpotential:

$$V_{act} = \eta_a + \eta_c = \frac{RT}{\alpha_a F} arcsinh\left(\frac{i}{2i_{0,a}}\right) + \frac{RT}{\alpha_c F} arcsinh\left(\frac{i}{2i_{0,c}}\right) \tag{S29}$$

(iii) Ohmic overpotential:

$$V_{ohm} = R_{ohm} I \frac{Il}{A(1-\varepsilon)^{1.5}} \tag{S30}$$

(iv) Mass transport overpotential:

The mass transport overpotential comprises two distinct contributions: the diffusion overpotential V_{diff} and the bubble-induced overpotential V_{bub}. The diffusion overpotential arises from the limitation of reactant transport through the anode and

cathode. In contrast, the bubble overpotential is predominantly on the anode side, where the accumulation of oxygen bubbles impedes the supply of liquid water to the catalyst sites.

$V_{mass} = V_{diff} + V_{bub}$

$$V_{diff} = \frac{RT}{4F} ln\left(\frac{c_{O_2}}{c_{O_2,0}}\right) + \frac{RT}{2F} ln\left(\frac{c_{H_2}}{c_{H_2,0}}\right) \quad \text{(S31)}$$

$$V_{bub} = \frac{RT}{4F} \ln\left(\frac{1}{\left(1 - s_{O_2,\,ACL}\right)^{n_s}}\right) \quad \text{(S32)}$$

The oxygen and hydrogen concentrations at the CLs are denoted by c_{O_2} and c_{H_2}, respectively, with $c_{O_2,0}$ and $c_{H_2,0}$ representing their corresponding reference concentrations. The average oxygen gas saturation at anode catalytic layer is expressed as $s_{O_2,\,ACL}$. The exponent n_s, referred to as the coverage coefficient, reflects the influence of gas or water saturation under high current density conditions and is assigned a value of 3.

■ Supporting Figures

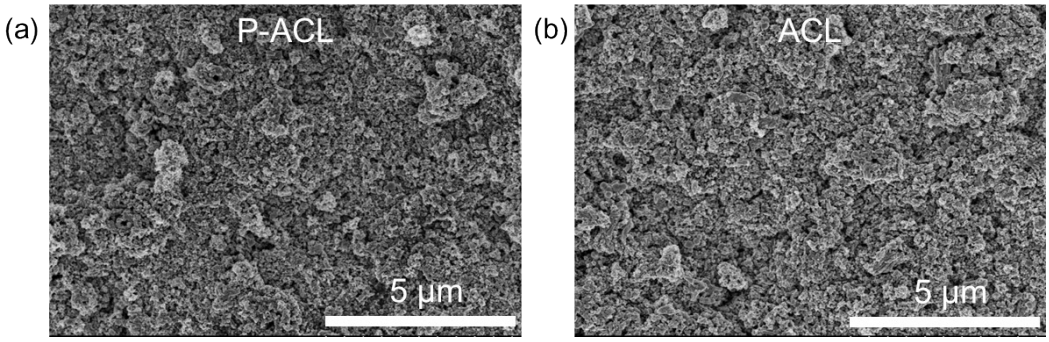

Figure S1. SEM image of P-ACL and ACL surface.

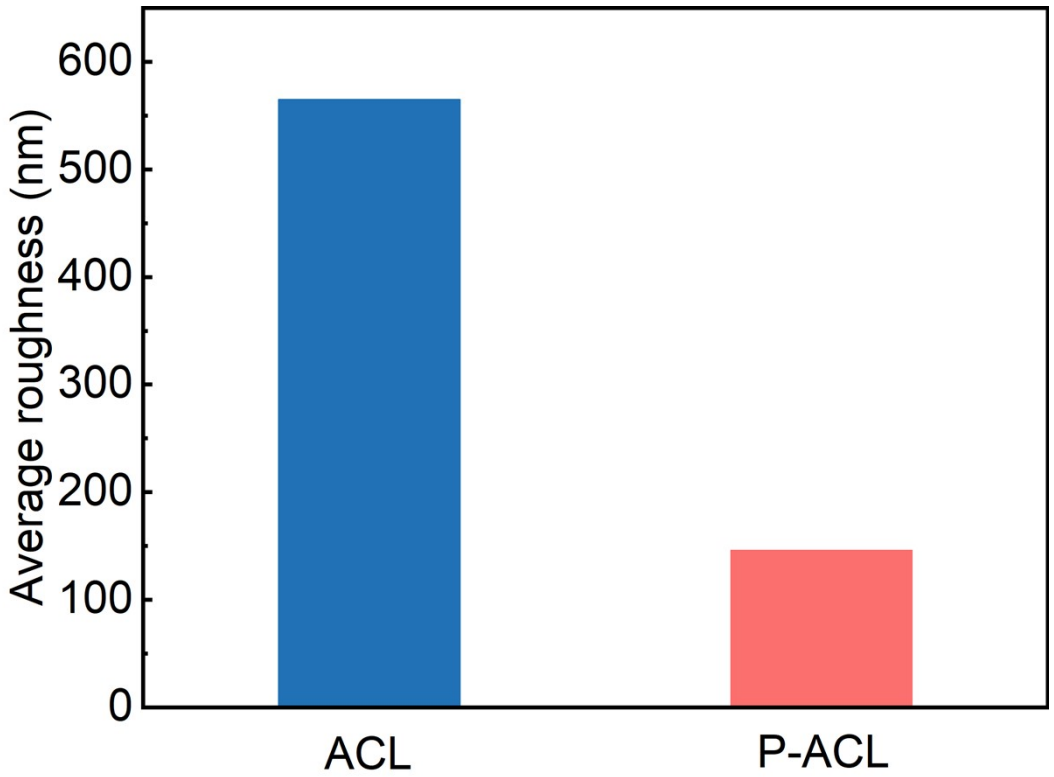

Figure S2. Average roughness of P-ACL and ACL.

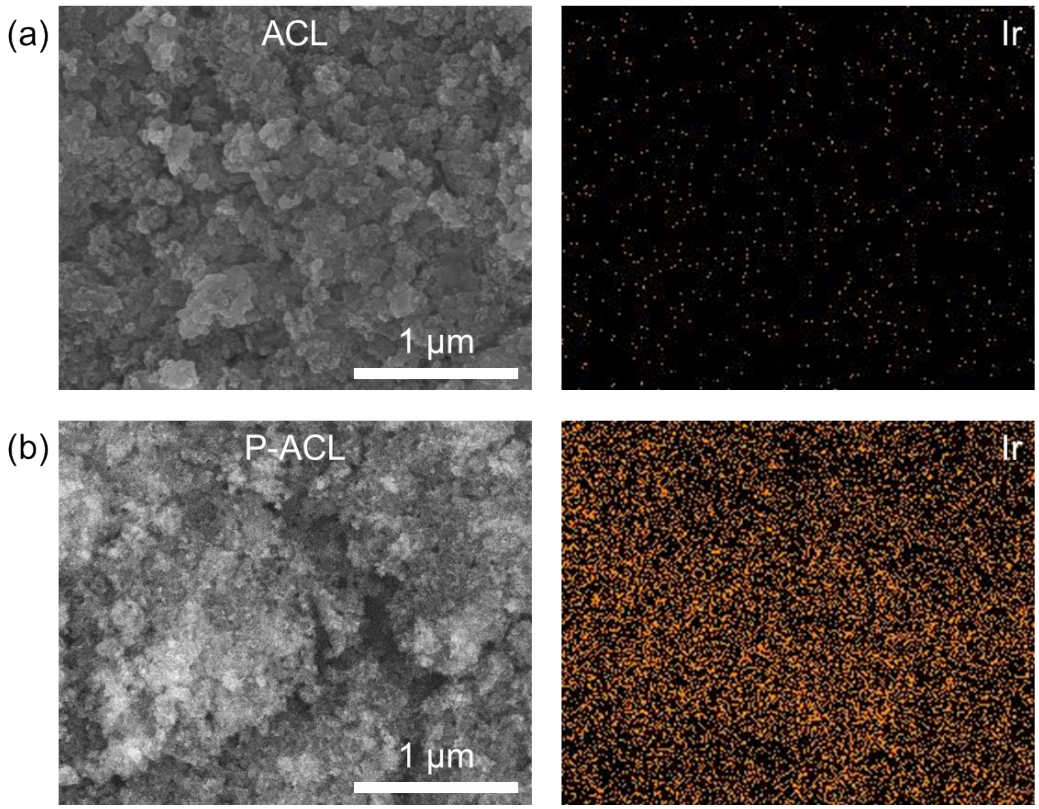

Figure S3. Average roughness of P-ACL and ACL.

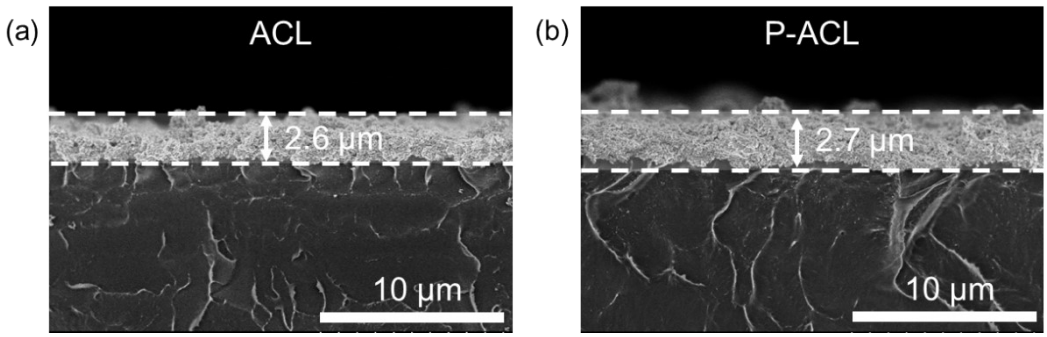

Figure S4. SEM image of P-ACL and ACL cross-section.

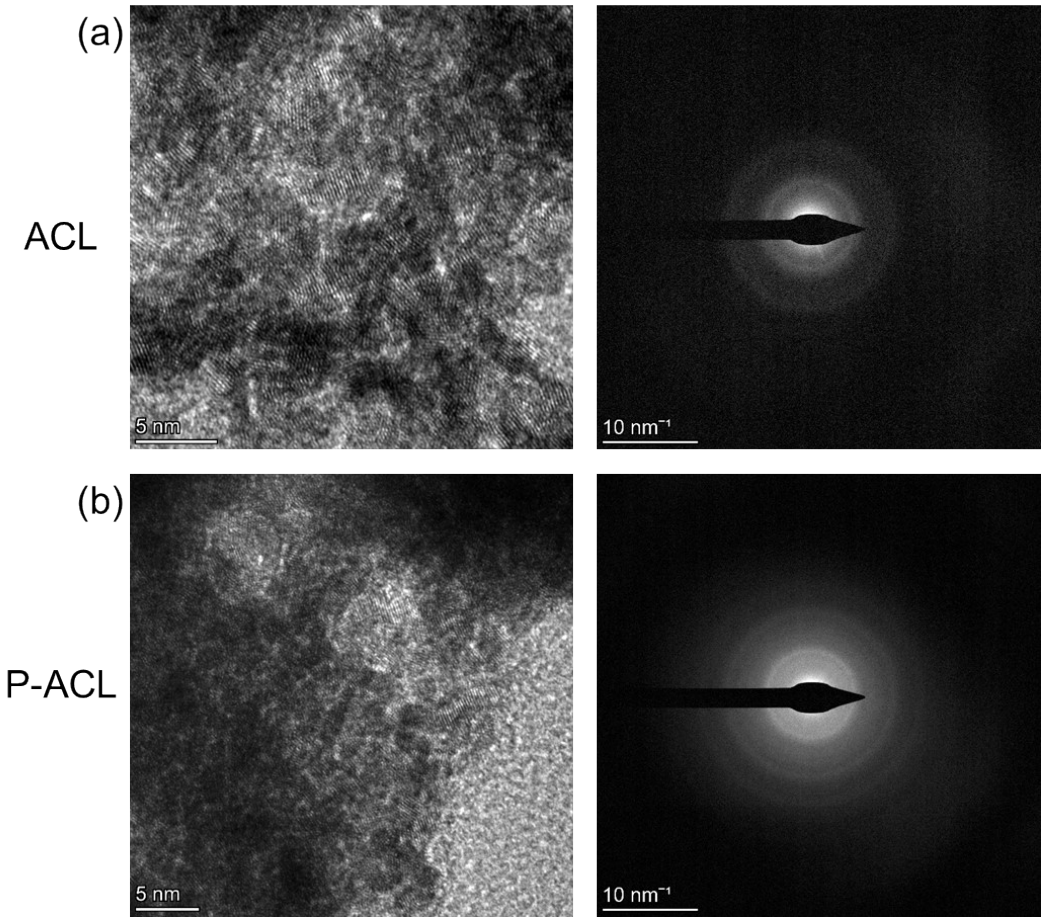

Figure S5. High-resolution transmission electron microscopy (HRTEM) images and corresponding selected area electron diffraction (SAED) patterns of IrO_2 catalysts in the ACL and P-ACL.

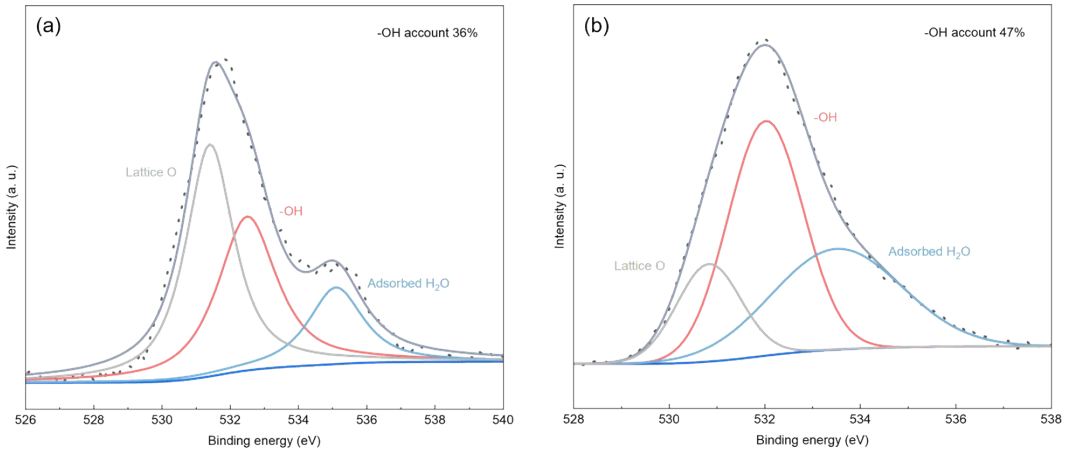

Figure S6. High-resolution XPS O 1s spectra of the anode catalyst layer (a) before and (b) after O_2 plasma treatment.

XPS O 1s spectra of the catalyst layers were deconvoluted into three main components: lattice oxygen (~530.5 eV), surface hydroxyl groups (-OH, ~532.0 eV), and adsorbed water (~534.5 eV). As shown in Figure S6, the relative content of surface -OH groups increased significantly from 36% in the pristine anode catalyst layer to 47% after O_2 plasma treatment.

This notable increase in surface hydroxyl density plays a critical role in enhancing proton transport within the catalyst layer. The introduced -OH groups can act as additional proton hopping sites and improve the hydrophilicity of the catalyst surface, facilitating the formation of more effective proton-conducting pathways at the catalyst-ionomer interface. Consequently, this leads to reduced mass transport resistance and improved overall PEMWE performance, particularly under high current densities where proton transport becomes more critical.

The correlation between elevated surface -OH content and enhanced proton conduction is consistent with previous reports on surface-modified electrocatalysts, where hydroxyl-rich surfaces promote water dissociation and proton mobility.

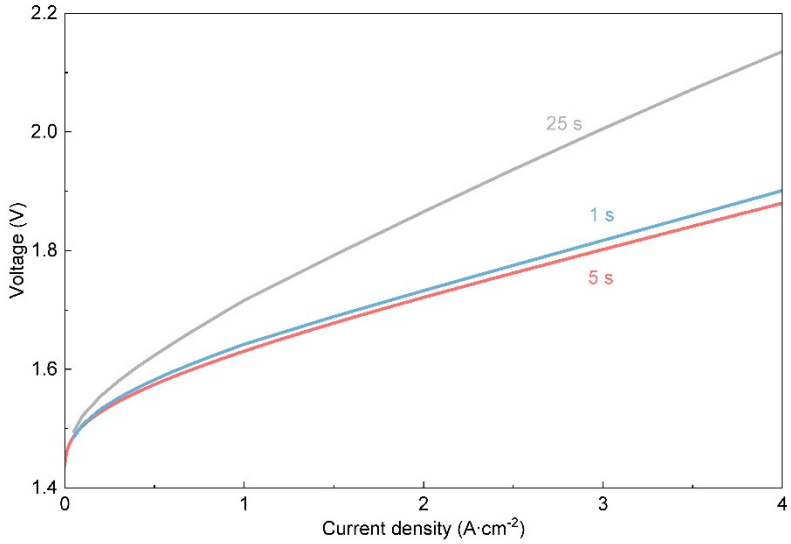

Figure S7. Polarization curves of ACLs treated with different plasma durations.

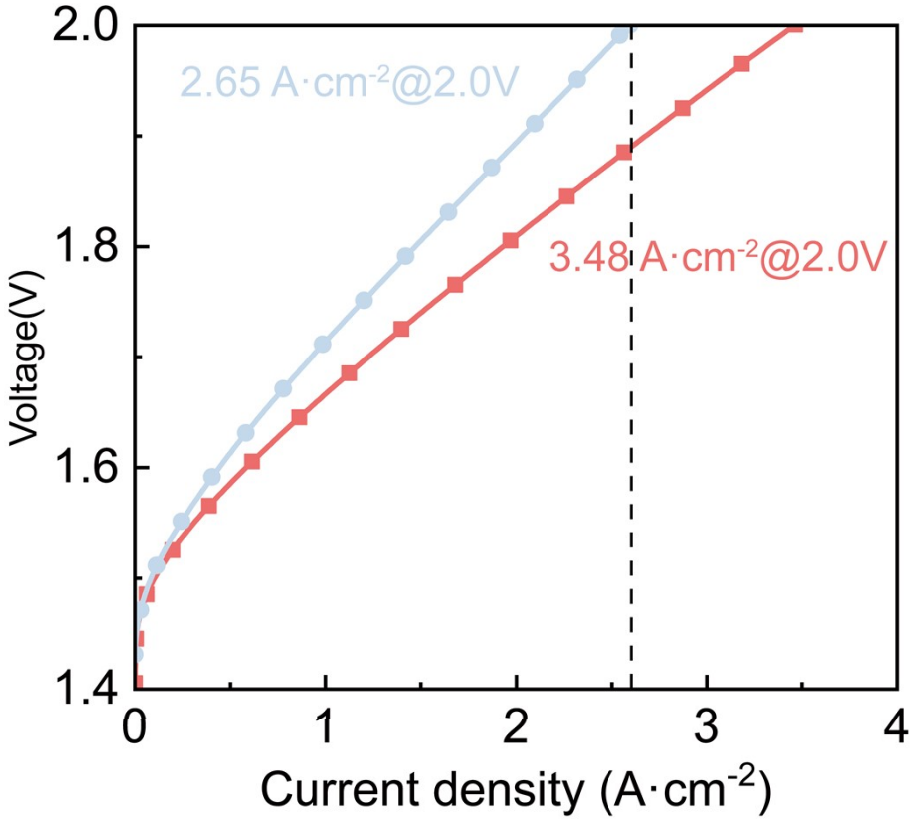

Figure S8. Polarization curves recorded at 70°C with Nafion N115.

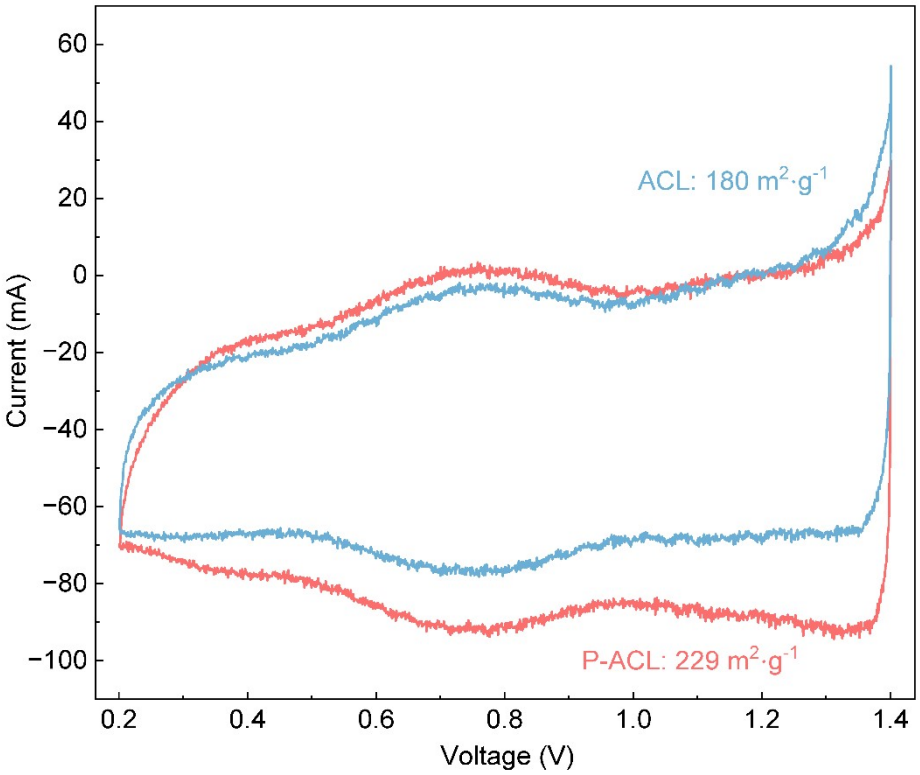

Figure S9. CV curves recorded at 70°C with Nafion N212.

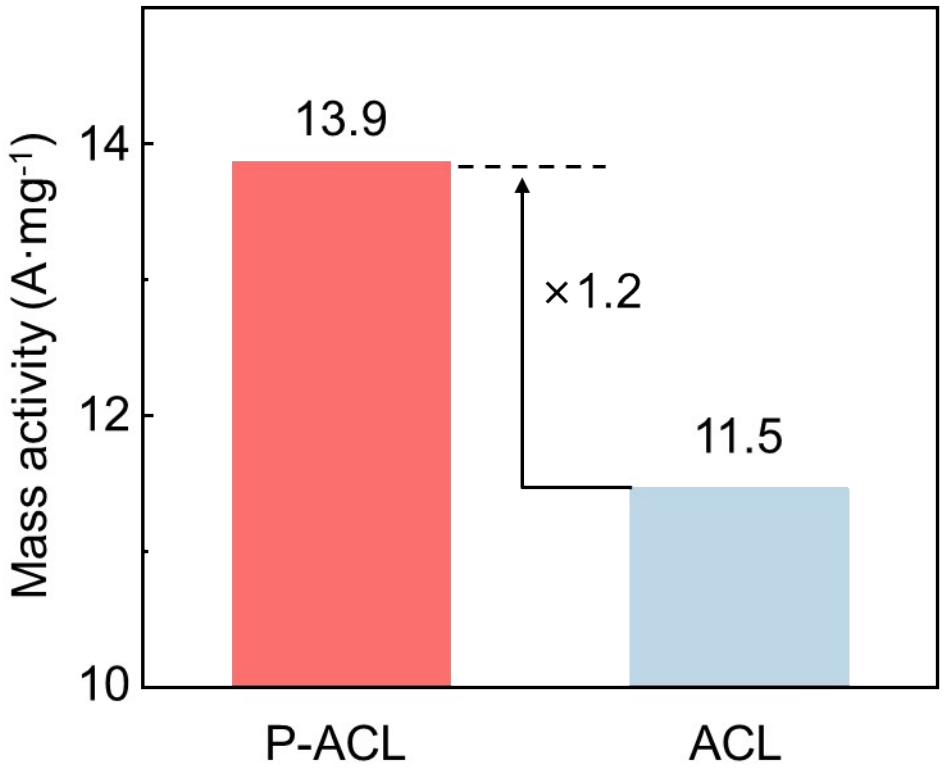

Figure S10. Mass activity of ACL and P-ACL.

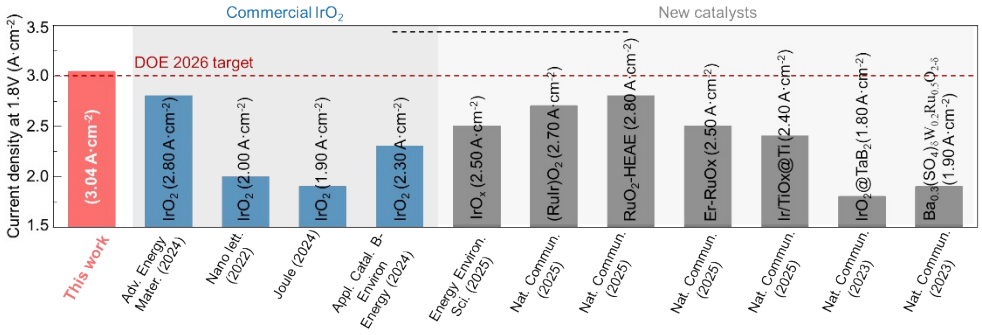

Figure S11. Benchmarking of current density achieved at 2.0 V against state-of-the-art Ir-based anodes reported in recent literature and commercial IrO_2.

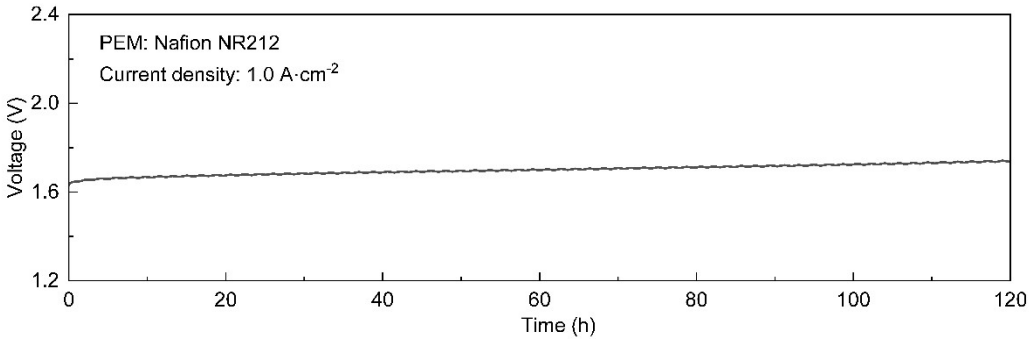

Figure S12. Stability test of PEMWE at 1 A·cm^{-2}.

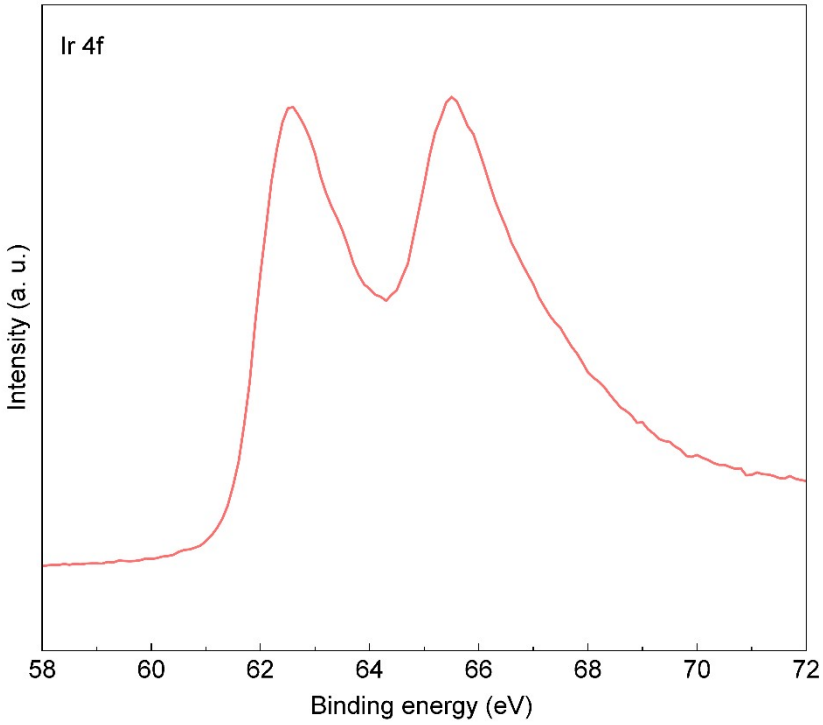

Figure S13. Ir 4f XPS spectrum of the plasma-treated catalyst after the 120-hour stability test, showing characteristic IrO_2 doublet peaks.

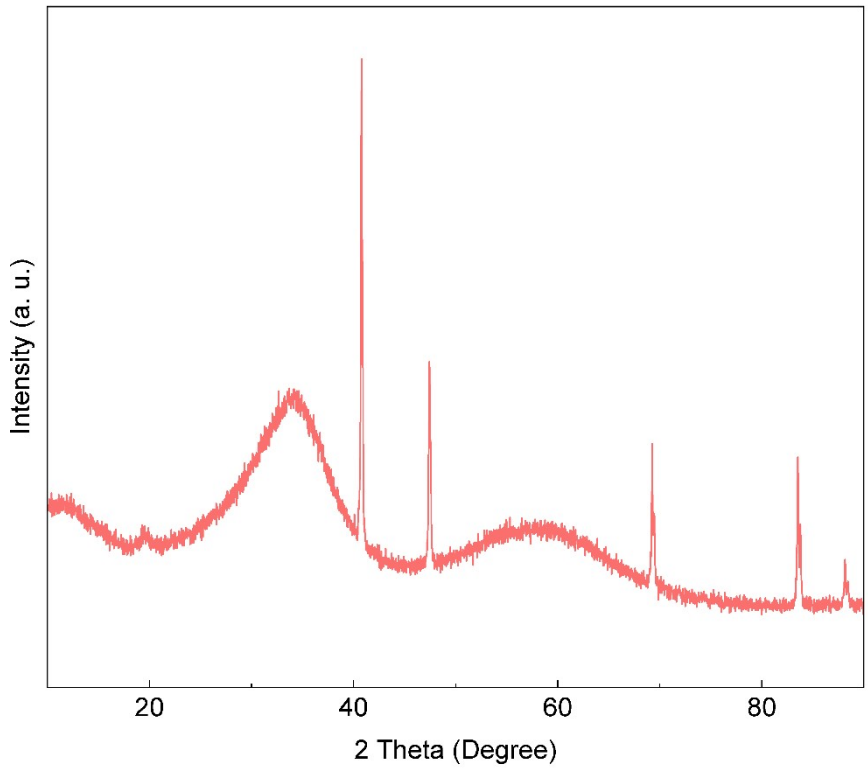

Figure S14. XRD pattern of the O_2 plasma-treated catalyst after the 120-hour stability test at 1.0 A·cm^{-2}.

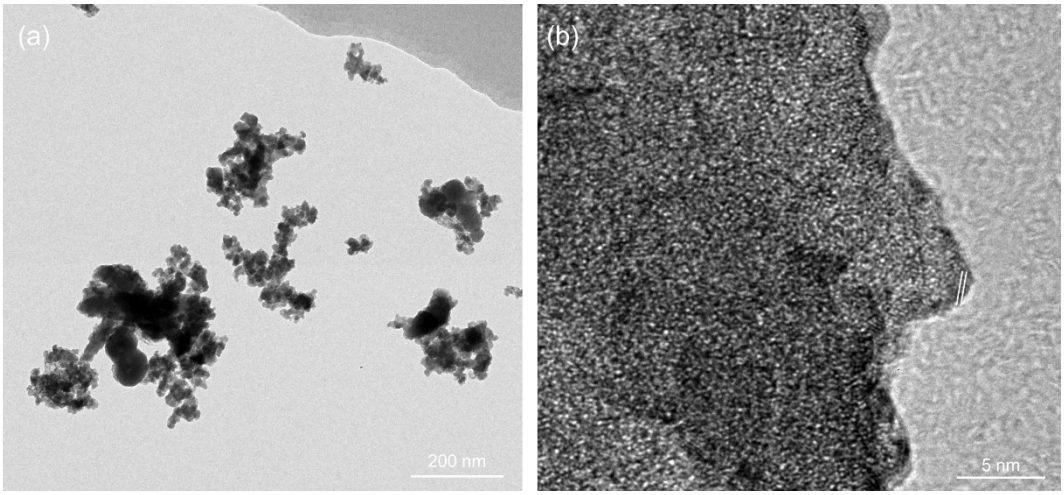

Figure S15. TEM images of the plasma-treated catalyst after the 120-hour stability test. (a) Low-magnification view and (b) high-resolution TEM image.

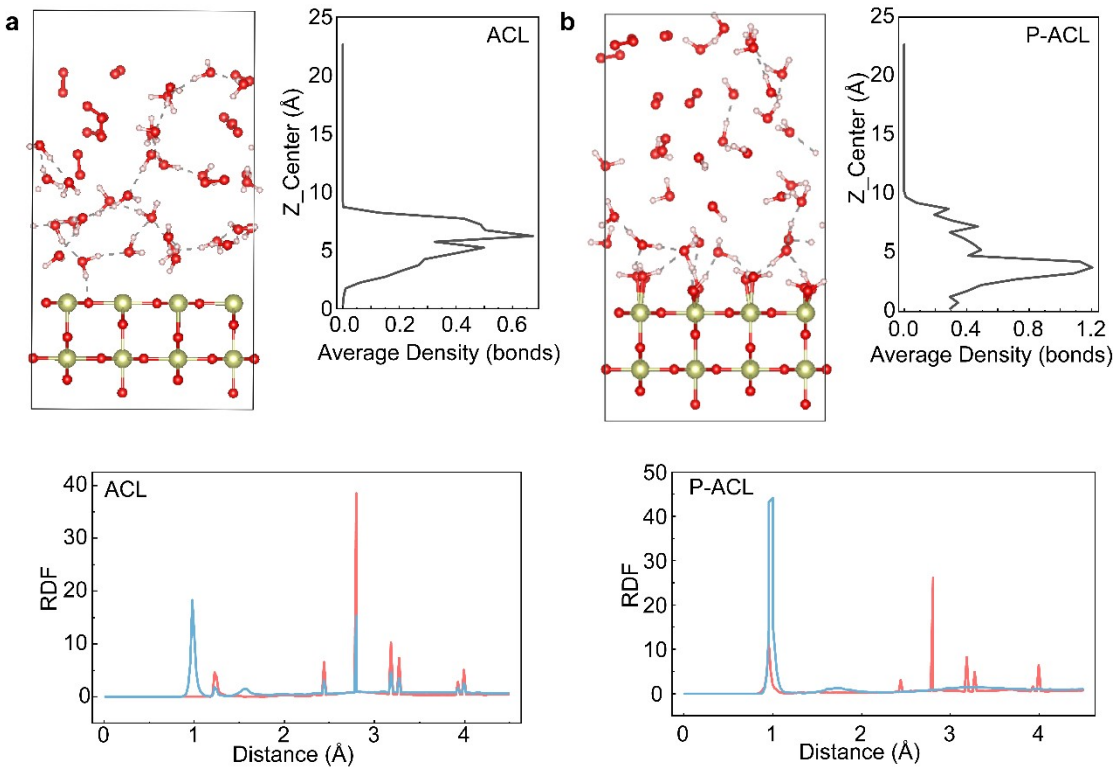

Figure S16. Microscopic mechanism of mass transport. (a) AIMD simulation model and average H-bonds density, (b) pair distribution function.

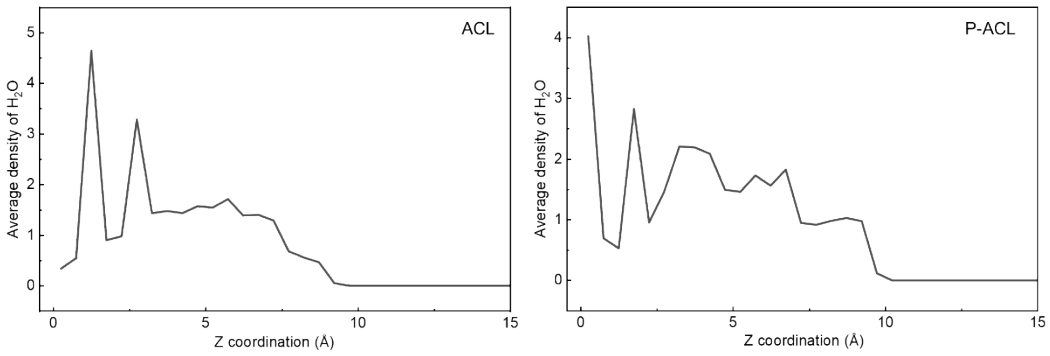

Figure S17. Average density of H_2O in the surface of ACL and P-ACL

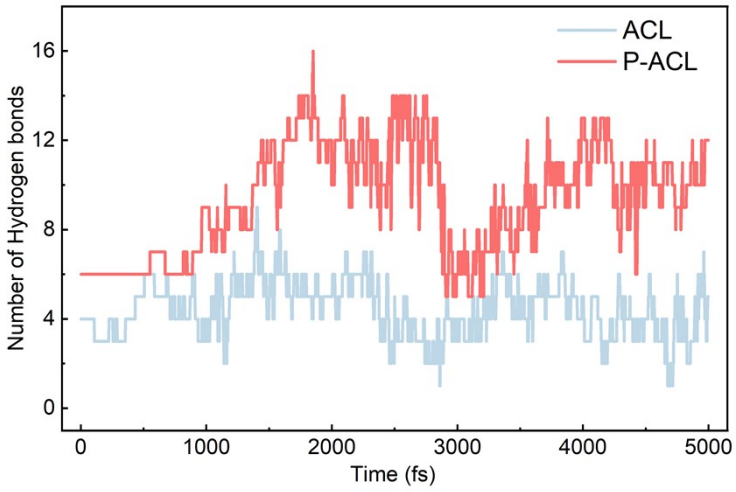

Figure S18. Number of H-bonds.

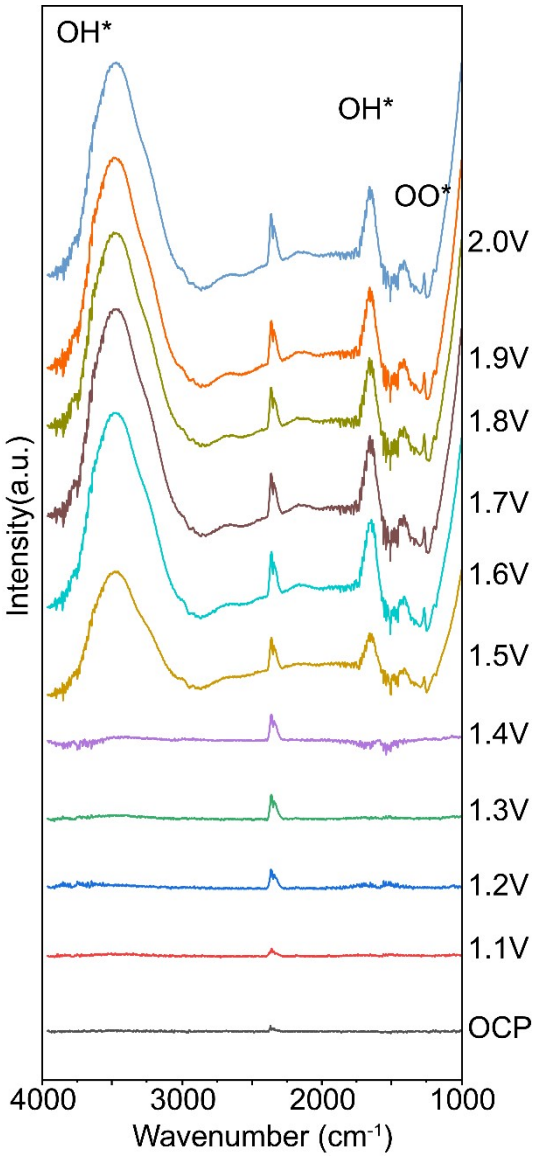

Figure S19. *In situ* ATR-SEIRAS difference spectra of P-ACL collected in 0.5 M H_2SO_4 under stepped potentiostatic OER conditions.

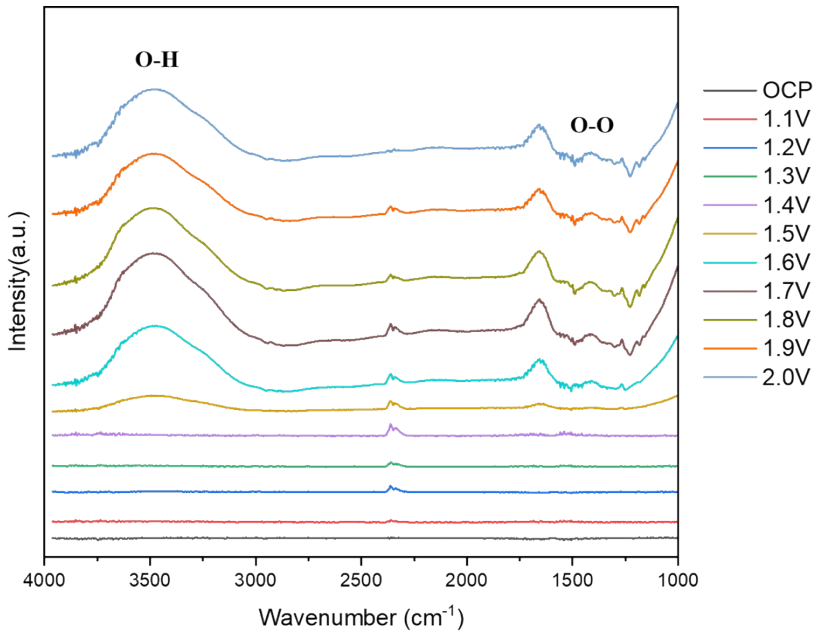

Figure S20. *In situ* ATR-SEIRAS difference spectra of ACL collected in 0.5 M H_2SO_4 under stepped potentiostatic OER conditions..

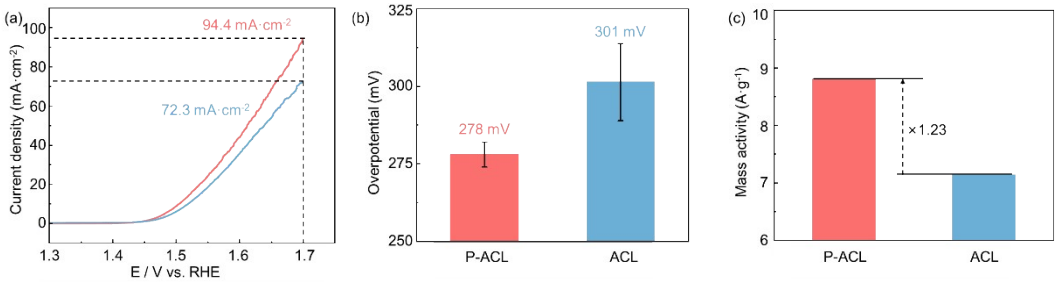

Figure S21. Three-electrode performance and microscopic mechanism of P-ACL and pristine ACL. (a) IR-corrected LSV curves, (b) overpotential at 10 mA·cm^{-2}, (c) mass activity.

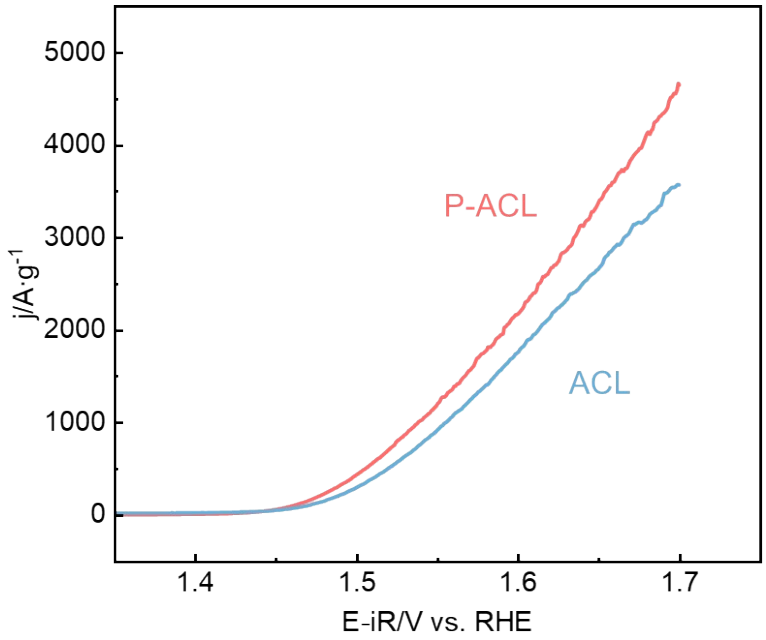

Figure S22. Mass-normalized LSV of ACL and P-ACL.

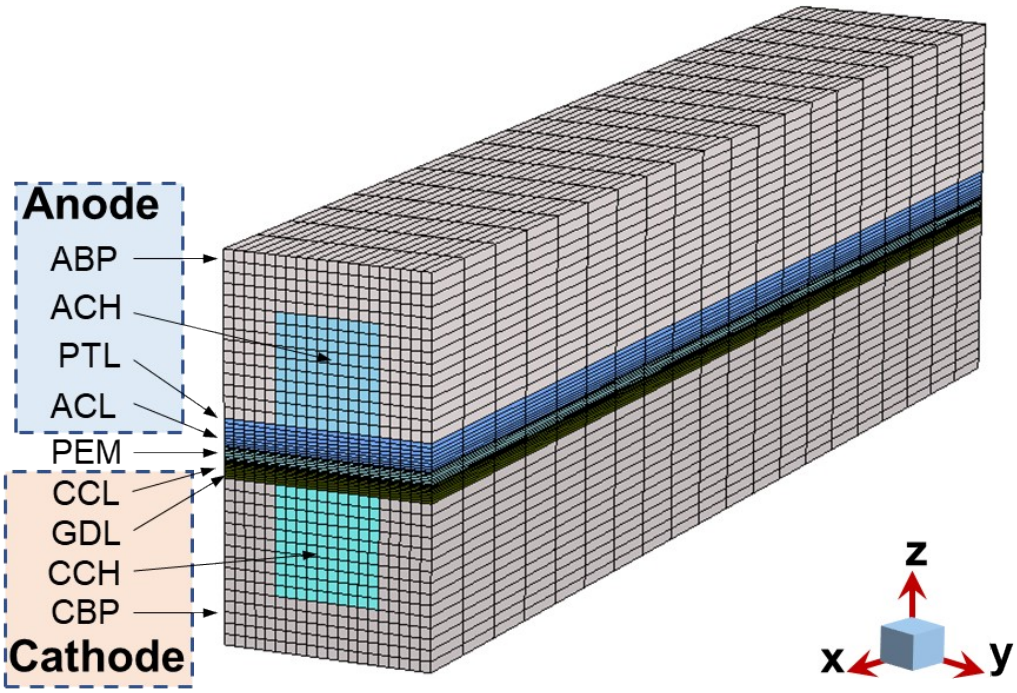

Figure S23. 3D computational domain and mesh.

The model integrates multiphase flow, electrochemical reactions, and mass transport with considering the hydrogen crossover. The key structural components including the proton exchange membrane (PEM), catalytic layers (CLs), porous transport layer (PTLs), and flow channel (CHs). The model was parameterized and validated against experimental data (Figure S13). Critical inputs such as the MEA configuration, catalyst loading, ionomer fraction and ACL thickness were derived from experimental measurements. A voltage sweeping from 1.2 V to 2.0 V with a 50-mV increment was simulated. The resulting polarization curve shows good agreement with experimental data, with the agreement improving at higher current densities. The maximum discrepancy, observed at the initial low-current stage and likely attributable to measurement uncertainties under minimal current flow, remains below 10%. The error falls within 2% for current densities exceeding 0.5 $A \cdot cm^{-2}$. Further validation was performed by comparing the simulated and experimental voltage loss contributions (kinetic, ohmic, and mass transport) at 2.0 A cm^{-2}, which showed consistent alignment, confirming the model's reliability (Figure S14), and the detailed data is shown in the Table S4.

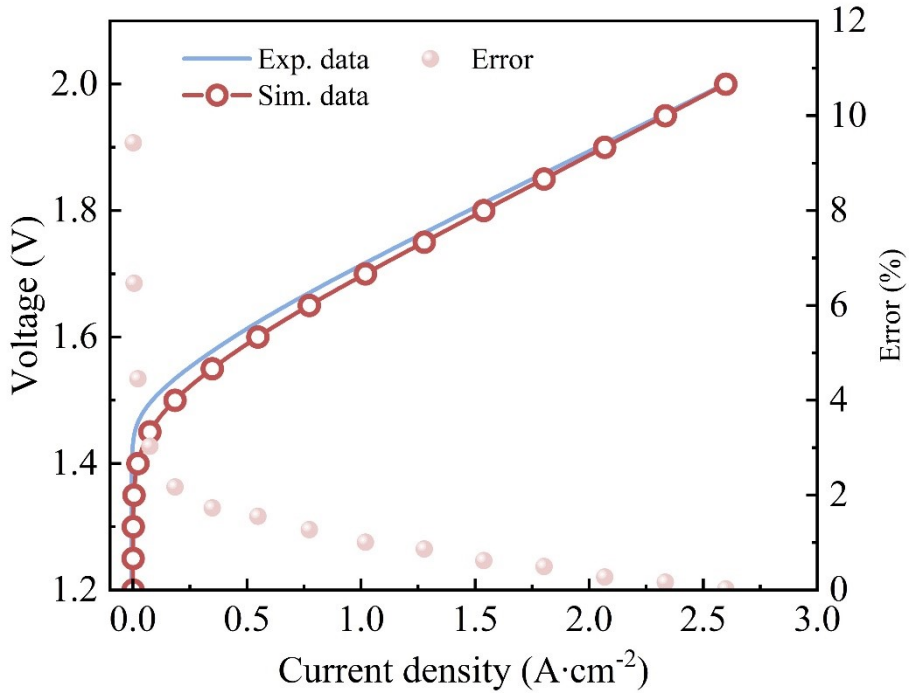

Figure S24. Validation of the PEMWE model through comparison of simulated and experimental polarization curves.

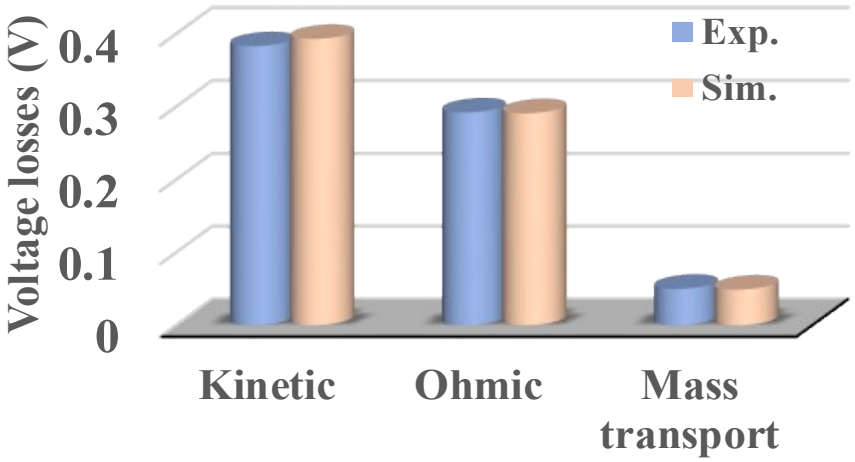

Figure S25. Comparison of voltage loss contributions.

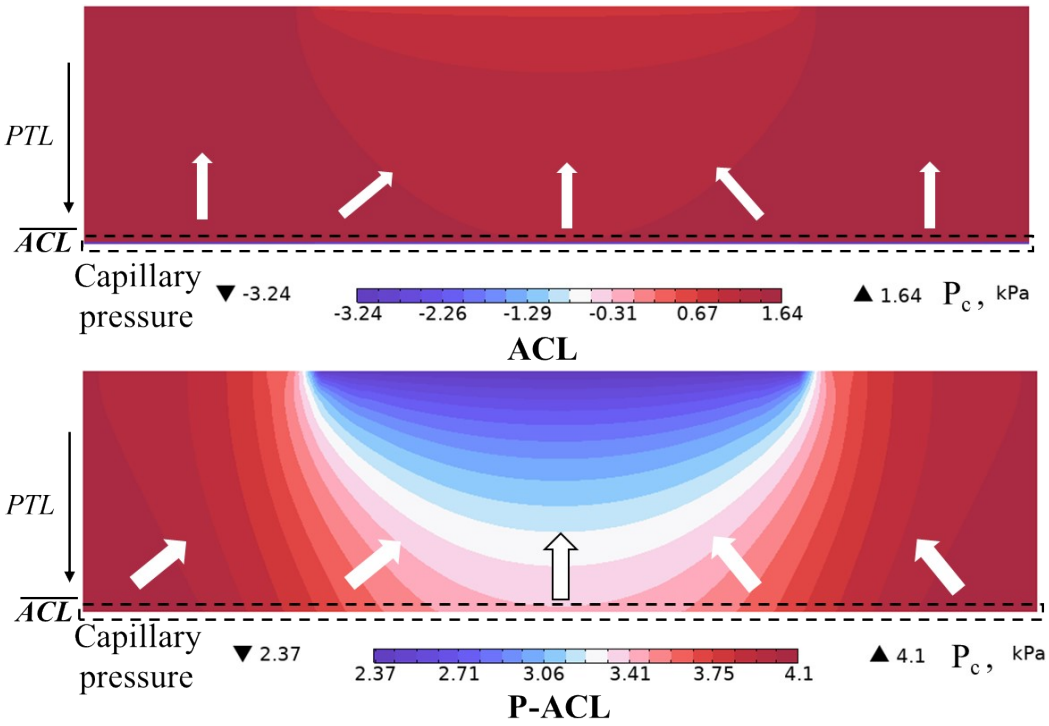

Figure S26. Capillary pressure distribution of ACL and P-ACL.

Table S1. Geometry parameters.

Parameters	Value
Single channel length (mm)	25
Single channel width (mm)	1
Single channel height (mm)	1
Bipolar plate width (mm)	0.5
Bipolar plate height (mm)	2
PTL thickness (μm)	250
GDL thickness (μm)	250
CLs thickness (μm)	1.5/5
PEM thickness (μm)	127
Cat. Loading (mg cm^{-2})	0.5/0.2
Mass fraction ion.	0.143/0.167
Transfer coefficient	0.5/0.5
PTLs porosity	0.5
Permeability of PTL/CL (m^2)	$1x10^{-12}$/$1x10^{-13}$
Conductivity of PTLs/CLs/BPs (S m^{-1})	$1x10^4$ /$5x10^3$/2 $x10^4$
PTL Contact angle (º)	80
ACL Contact angle (º)	110
P-ACL Contact angle (º)	70

Table S2. Boundary and initial conditions.

Fluid transport: mass and momentum conservation	
Anode channel inlet	$u_a = u_{a,in}$
Anode/Cathode channel outlet	$p_a = p_c = 1\ bar$
Species transfer of gas	
Anode/Cathode channel inlet	$c_{0,O_2} = c_{0,H_2} = 0\ mol/m^3$
Anode/Cathode channel outlet	$\vec{n} \cdot D_i \nabla c_i = 0$
Charge transport and conservation	
Anode end plate	$\phi_s = V_0$
Cathode end plate	$\phi_s = 0\ V$
Energy conservation	
Anode channel inlet	$T_{a,in} = T_{c,in} = 353.15\ K$
External walls	$-\vec{n} \cdot q = 0$
Liquid water saturation conservation	
Anode channel inlet	$s_{a,in} = 0.9$, $s_{c,in=}\ 0.2$
Anode/Cathode channel outlet	$-\vec{n} \cdot D_i \nabla s_i = 0$

Table S3. Source terms within each region of the computational domain.

Source	PEM	ACL	CCL	PTL
S_l	—	$-\frac{R_a M_{H_2O}}{2F} + S_l$	$S_{vs}M_{H_2O} - S_{v\lambda}M_{H_2}$	$S_{vs}M_{H_2O}$
S_g	—	$\frac{R_a M_{O_2}}{4F} - S_{vs}M_{H_2O}$	$\frac{R_c M_{H_2}}{2F} - S_{vs}M_{H_2O}$	$-S_{vs}M_{H_2O}$
S_c	—	$\frac{R_a}{4F}$	$\frac{R_c}{2F}$	0
S_e	0	R_a	$-R_c$	—
S_p	0	R_a	$-R_c$	—
S_T	$S_{T,JH}$	$S_{T,JH} + S_{T,m}$	$S_{T,JH} + S_{T,m}$	$S_{T,JH}$
S_λ	—	$S_{v\lambda}$	$S_{v\lambda}$	—

1 Table S4. Model variation for voltage losses.

Voltage losses (V)	Exp.	Sim.
Kinetic (V)	0.383	0.393
Ohmic (V)	0.292	0.291
Mass transport (V)	0.05	0.049

2